Single-dot absorption spectroscopy and theory of silicon nanocrystals

Ilya Sychugov,[1,*] Federico Pevere,[1] Jun-Wei Luo,[2] Alex Zunger,[3] and Jan Linnros[1]

[1]*Materials and Nano Physics Department, KTH–Royal Institute of Technology, Kista, Stockholm 16440, Sweden*

[2]*State Key Laboratory for Superlattices and Microstructures, Institute of Semiconductors, Chinese Academy of Sciences, P.O. Box 912, Beijing 100083, China*

[3]*Renewable and Sustainable Energy Institute, University of Colorado, Boulder, Colorado 80309, USA*

Photoluminescence excitation measurements have been performed on single, unstrained oxide-embedded Si nanocrystals. Having overcome the challenge of detecting weak emission, we observe four broad peaks in the absorption curve above the optically emitting state. Atomistic calculations of the Si nanocrystal energy levels agree well with the experimental results and allow identification of some of the observed transitions. An analysis of their physical nature reveals that they largely retain the indirect band-gap structure of the bulk material with some intermixing of direct band-gap character at higher energies.

Finite-sized nanostructures and bulk random alloys lack the translational symmetry of the underlying bulk-periodic solids they are drawn from. Therefore their wave functions represent a mix of bulk bands over different wave vectors and band indices [1,2]. The additional shift in energies present in nanostructures due to quantum confinement and enhanced many-electron interactions in confined space lead to clear spectroscopic manifestations in nanostructures relative to the reference bulk material [3]. This includes changing of a bulk indirect transition to a nanostructure quasidirect transition [4], as well as more exotic effects such as Coulomb and spin blockade, appearance of many-electron multiplets, violations of Hund's rule and the Aufbau principle, etc. [5]. The modern theory of nanostructures treats such single nanostructures atomistically as a giant molecule rather than via continuum-based effective mass methods [3,6]. However, such high-resolution theoretical calculations cannot be compared with experimental data from ensemble measurements, where size (and shape) dispersion even at a very small scale smears out discrete features both in emission and absorption. Single-dot spectroscopic techniques have been previously applied to self-assembled and colloidal direct band-gap material quantum dots (QDs) of III-V [5,7,8] and II-VI group elements [9]. They have indeed revealed, in conjunction with theory, significant novel nanostructure effects forming the basis for the current understanding of QD physics.

Experimentally, the spectrum of nanocrystals can be probed by emission and absorption spectroscopy. While the emission peak position corresponds to the effective optical band gap, the absorption measurements can provide information over a wide energy range, allowing for a more detailed comparison to calculations. So far only ensemble studies were performed on the absorption spectrum of Si nanocrystals by photoluminescence excitation (PLE) or transmission methods [10,11], preventing us from observing single Si nanodot features. PLE of individual quantum dots was demonstrated for direct band-gap materials [12–14], but it is much more difficult to perform on single Si nanocrystals due to their low emission rate, stemming from $\sim\mu$s exciton lifetimes [15]. At the same time, understanding the electronic structure of Si nanocrystals

relevant for light absorption is central to their application as phosphors [16], biolabels [17], sensitizers [18], downshifters [19], or photon multipliers [20].

In this Rapid Communication we report successful single-dot spectroscopy studies of silicon quantum dots, revealing the absorption states above the emission level. The experimental difficulty of detecting weak PLE signals from single Si nanocrystals under varying excitations was solved by introducing a stable, focusable, and tunable light source to the sensitive detection system, as described in the Supplemental Material [21].

Previously we could access only the emission state of individual Si nanocrystals in photoluminescence [4,22] and decay measurements [15,23]. The Si quantum dot origin of the emission was evidenced by the observed variation in emission peak position and lifetime, the sharp narrowing of the linewidth at lowered temperature, a signature of biexciton recombination at high excitation, and a Si transverse optical (TO)-phonon sideband in the spectra. Here we present spectroscopic results over a broad energy range (1.5–2.0 eV above the emission state) for Si nanocrystals. A typical spectrum is shown in Fig. 1 (circles, right), where several distinct absorption features can be identified, which are not seen in ensemble absorption measurements (dashed line).

We have calculated the energy states and absorption spectra of Si nanocrystals using a set of well-tested theoretical tools based on the empirical pseudopotential method [25]. By employing this atomistic method one no longer needs to use the effective-mass based (continuum) approximations, with their significant flaws [26–28]. Unlike the (atomistic) local density approximation (LDA) methods, the theory discussed here is free from the well-known LDA errors on band gap and effective masses [29], both rather detrimental to obtaining a physically correct description of quantum confinement. In this "modern theory of QDs" one includes a fairly complete description of single-particle effects (multiband interactions; multivalley coupling; spin-orbit interactions; surface or interface effects) [3,28,30]. We solved the atomistic Schrödinger equation explicitly for QD architecture consisting of a thousand to multiple millions of atoms, with the atoms located at specific positions, each carrying its own (screened) pseudopotential [25]. These semiempirical pseudopotentials were obtained
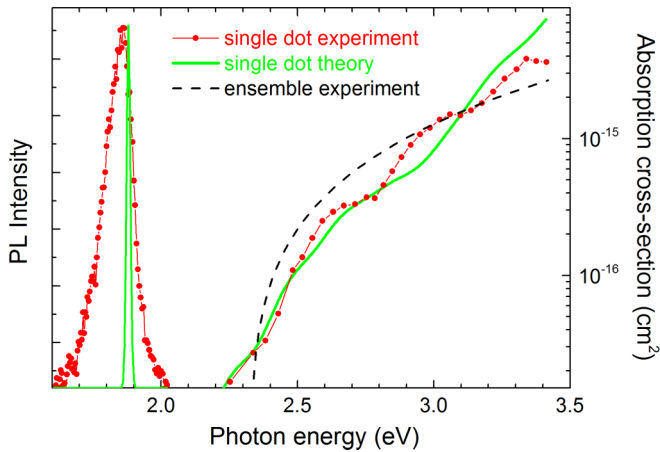
---

*Corresponding author: ilyas@kth.se

FIG. 1. Comparison of the experimentally obtained absorption curve (red circles to the right) with a calculated one (broadening 50 meV) for a ∼3 nm diameter Si nanocrystal (green curve) exhibiting best agreement. The room-temperature photoluminescence spectrum (PL) of this nanodot is presented as red circles to the left. The PL peak position is close to the calculated band gap (green peak at 1.88 eV). A typical featureless ensemble absorption [24] is also given for comparison (dashed line).

from fitting to the experimental parameters of the bulk material [29]. The no-phonon optical absorption spectrum in a single-particle basis was then calculated using Fermi's golden rule, where many-body effects are solved using a configuration interaction (CI) approach [3]. Such an approach will help us to understand the origin of the spectral features observed experimentally in Si quantum dots. This theoretical method is summarized in the Supplemental Material and has been tested extensively over the past two decades for a broad range of spectroscopic quantities in colloidal as well as self-assembled nanostructures from the atomistic point of view [3,25–30].

In this work, theory and experiment are compared in a wide spectral range, from the emission peak position to the highest-energy absorption, pertaining to direct transitions. This is illustrated in Fig. 1 by comparing the measured (red) and the calculated (green) absorption curves for a ∼3 nm Si nanocrystal. This nanodot has a calculated band gap of

∼1.88 eV (green peak), similar to the measured PL peak position of ∼1.86 eV (red peak). Indeed, one can notice a good agreement over nearly three orders of magnitude in absorption intensity, where a growing curve with several discernible steps is predicted and observed experimentally. In this way, single-dot spectroscopy and atomistic calculations allowed us here to identify and analyze light absorbing states in indirect band-gap material nanocrystals.

The samples were fabricated by etching and short oxidation of silicon-on-insulator (SOI) wafers resulting in close to spherical, as well as faceted, silicon nanocrystals in an amorphous oxide matrix [4,31]. A typical transmission electron microscopy (TEM) image of such nanocrystals is shown in Fig. 2 (left). Interplane distance analysis reveals no significant

FIG. 3. Typical (top) room-temperature and (bottom) low-temperature photoluminescence (linewidth indicated) and absorption spectra of two different individual silicon quantum dots. Four steps on the absorption curves can be distinguished and the black line is a fit based on four Gaussians (see text).
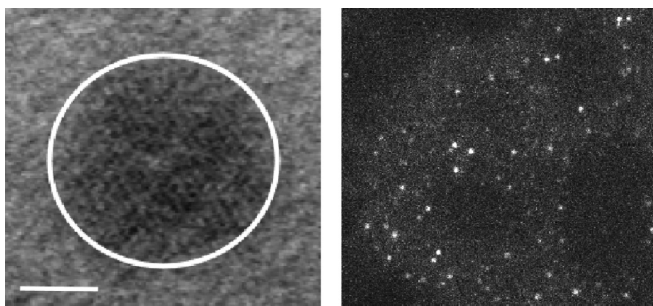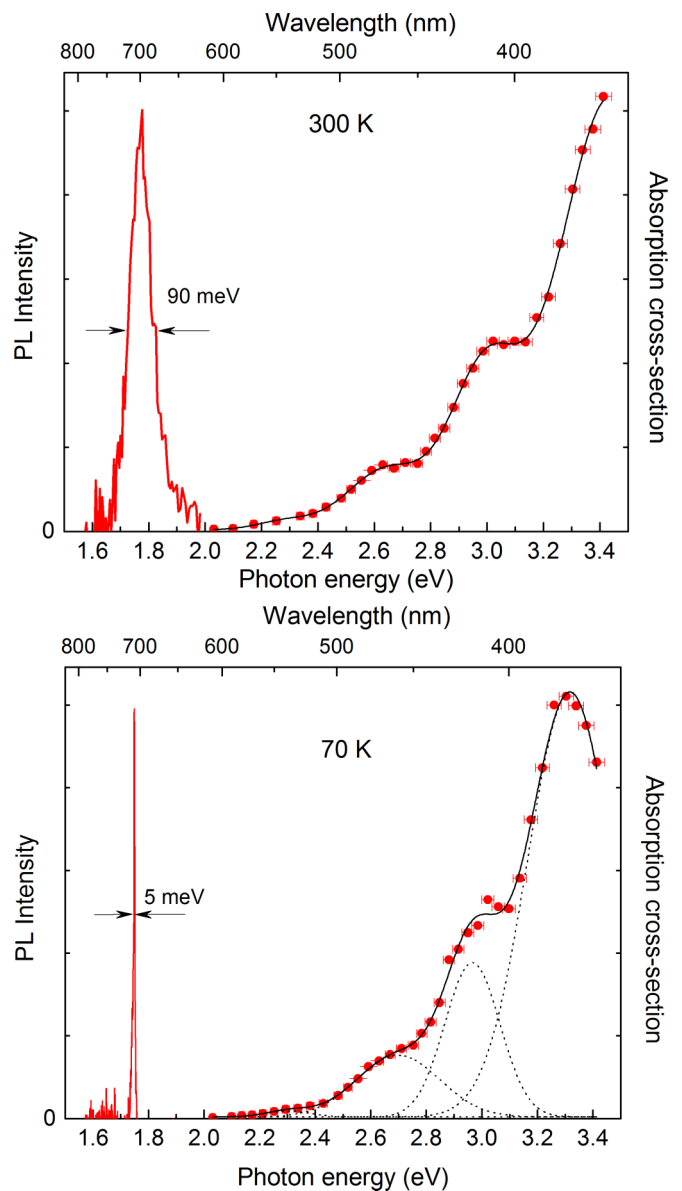

FIG. 2. Left: Cross-sectional TEM image of a silicon nanocrystal taken along the [110] direction from an SOI sample. Si (111) plane lattice fringes visible (scale bar 2 nm). Right: Photoluminescence image of ∼50 × 50 μm² sample area. Bright points correspond to luminescence from individual Si quantum dots, formed randomly in a thinned SOI layer.

TABLE I. Summary of the observed and calculated absorption peak parameters: E_0 is the peak position; ΔE is the full width at half maximum. Experimental peak parameters represent average over all dots measured at low temperature (see Table S1). Peak parameters for the theory curve are from the fitting shown in Fig. S2.

Parameter	Peak 1		Peak 2		Peak 3		Peak 4	
	E_0 (eV)	ΔE (meV)	E_0 (eV)	ΔE (meV)	E_0 (eV)	ΔE (meV)	E_0 (eV)	ΔE (meV)
Experiment	2.29	210	2.67	340	2.94	230	3.33	460
Theory	2.27	110	2.45	180	2.80	410	3.45	500

strain (Fig. S1). The PLE measurements were carried out in a microphotoluminescence setup using epifluorescence excitation geometry. A laser-driven xenon lamp with an attached monochromator was used as a wavelength-tunable excitation source from 350 to 620 nm with $\sim$6 nm spectral resolution. The nanocrystals emitting in the range from 1.7 to 1.9 eV could be probed in this experiment and only nonblinking particles were considered. For low-temperature measurements the samples were mounted on a cold finger of a cryostat, and a typical PL image of such samples is shown in Fig. 2 (right). Absorption curves were obtained by correcting the detected PL signal to the excitation intensity for every wavelength. Absolute values of the absorption cross section were found using luminescence rise time measurements under a modulated laser diode excitation at 405 nm. Since the exact information on the nanocrystal shape and size is difficult to obtain, measured emission peak positions served as an experimental input to the calculations, indicating a typical size of the nanocrystals studied in this work of $\sim$3 nm. Further experimental details are provided in the Supplemental Material.

Figure 3 shows typical absorption spectra recorded at 300 K (top) and 70 K (bottom), together with the corresponding emission lines for two different nanodots. Altogether, nine such silicon nanocrystals were probed, revealing a similar pattern in the absorption curves, which consists of several steps. One can identify four absorption peaks from the multicomponent Gaussian fitting (black curves in Fig. 3), and the averaged peak parameters are presented in Table I (a breakdown over individual dots is given in Table S1). It is seen from Fig. 3 that temperature has little effect on the absorption curve, although at 70 K the first peak at $\sim$2.3 eV becomes somewhat clearer. The emission linewidth narrows from $\sim$100 meV at 300 K to $\sim$5 meV at 70 K, which is as sharp as we have ever observed for a Si QD at

this temperature and clearly less than $k_B T$. This effect was studied in detail previously, where it was attributed to the exciton phonon coupling [22]. The calculated absorption peak parameters for a $\sim$3 nm nanodot (obtained by deconvolution of the calculated curve from Fig. S2) are also included in Table I for comparison, revealing reasonable quantitative agreement with the experiment.

The absolute values of the absorption cross section, measured for three nanocrystals at 300 K, yielded values in the range $0.8 - 1.9 \times 10^{-15}$ cm^2 under 405 nm excitation. Such values are typical for Si nanocrystals in an oxide matrix [32]. Thus we can define the average value of the absorption cross section at this excitation energy (3.06 eV) as $\sigma_{avg} \approx 1.5 \times 10^{-15}$ cm^2, which was used to normalize the measured curve in Fig. 1. Some variations of the absorption cross-section values were found even for nanocrystals with a similar emission energy. As revealed by the shape-dependent calculations shown in Fig. 4 (left), it can be attributed to slight structural nonuniformities among the probed nanoparticles. Such shape variations can also explain the small discrepancies in the calculated curves with the experiment (cf. Table I and Fig. 1), where the exact shape of the probed nanocrystals may vary slightly from dot to dot.

After establishing good agreement between the measured and calculated transition energies, we can interpret theoretically the origin of the transitions. For that we performed many-body calculations, which include electron-hole Coulomb interactions and correlation effects as described in the Supplemental Material. The resulting excitonic spectrum for nanodots with slightly different geometries is shown in Fig. 4 (right), where individual transition peaks are marked for the 3 nm nanodot. We identify the first peak in the experimental absorption curve at $\sim$2.3 eV (cf. Fig. 3) as a combination of $S_h \rightarrow D_e$ and $P_h \rightarrow P_e$ transitions (S, P, and D are notations
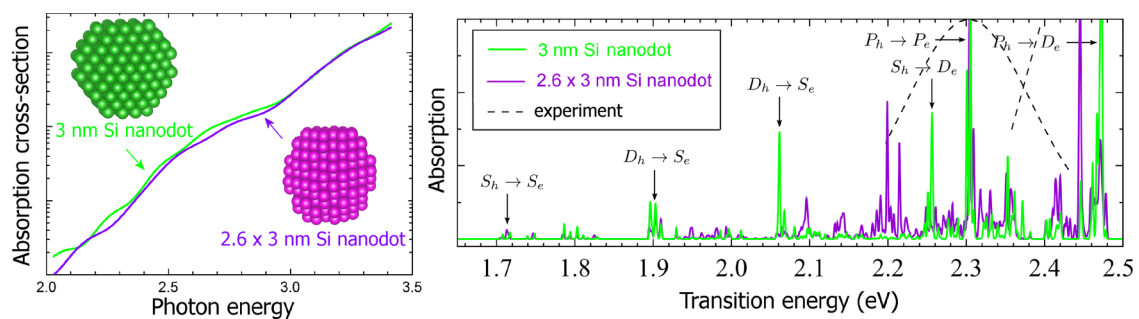

FIG. 4. Left: Calculated absorption curves (broadening 50 meV) for a nanodot of $2.6 \times 2.6 \times 3$ nm dimensions (purple) and for a 3 nm diameter nanocrystal (green) on a log scale. Small shape variations slightly modify the absorption curve. Right: The exciton spectrum counterpart including many-body effects (broadening 1 meV). Dashed lines represent the experimentally obtained peaks.
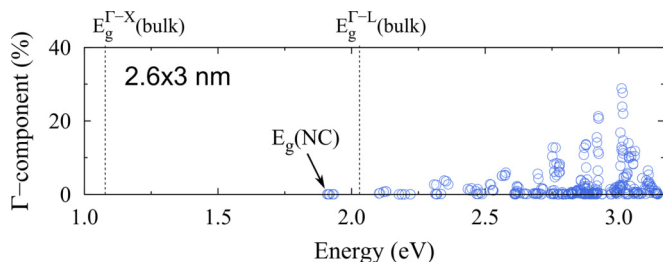
FIG. 5. Projections of the calculated conduction band states to bulk directlike Bloch functions for a $2.6 \times 2.6 \times 3$ nm Si nanodot in oxide matrix. The intermixing of Γ and X components is stronger for higher energy.

of the envelope functions with orbital angular momentum 0, 1, and 2 for holes and electrons in a silicon quantum dot). The next broad peak at ~ 2.65 eV partially consists of the $P_h \rightarrow D_e$ family of transitions. Higher-energy states of such nanodots were not analyzed in detail as they appear to consist of several mixed transitions from numerous, densely spaced electron and hole states. These states are highly quasidegenerate [25], and transitions between different sublevels result in broad experimental peaks (shown as a dashed line in Fig. 4, right), limited by the probe energy resolution and thermal broadening.

When analyzing these results we first notice that the absorption is very weak in the vicinity of the emission line (cf. Fig. 3). Indeed, the signal count rate for red light excitation was about two orders of magnitude lower than for blue light excitation, requiring a much longer time to get a measurable signal. To understand the nature of the absorbing states we calculated the conduction state wave-function projections to bulk Bloch functions (see the Supplemental Material). Since the initial valence band states are mostly localized around the Γ point, the Γ component of these projections represents the direct band-gap character of the transitions (Fig. 5). Indeed, the levels close to the emission energy retain the indirect nature of the bulk Γ'_{25}-Δ_1 band gap (only $\sim 10^{-3}$ admixture of the Γ component), while at higher energies a strong intermixing of X and Γ states occurs (up to 30%). This situation is different from direct band-gap quantum dots, where strong direct band-gap related absorption peaks are located right next to the emission line [12–14].

This fact has a positive effect for the application of Si nanocrystals as phosphors in white-light emitting devices [16]. Indeed, from Fig. 3 one can see that within at least ~ 300 meV next to the emission peak (~ 110 nm for 1.8 eV) Si nanocrystals are nearly absorption free. The optimum positions of the trichromatic source for the generation of white light with a high color rendering index are at 450, 540, and 610 nm [33]. While the blue light in most modern white light-emitting diodes (LEDs) comes from an (In)GaN diode, the red and green bands originate from light converting phosphors. The ~ 70 nm difference between the red and green bands is well within the poor absorption interval of Si nanocrystals. Thus the reabsorption for the green-red phosphor combination, which is a common problem for direct-band-gap nanocrystals [34], can be significantly reduced. Second, quantum dots have been recognized as superior biomarkers for multiplexing applications in biolabeling [35]. Here we note that the absorption at high energies is quite strong for Si nanocrystals due to the direct band-gap character admixture (Fig. 5), regardless of the emission energy, as shown recently for ensembles of ligand-passivated Si nanocrystals [36]. Such a large Stokes shift makes these nanoparticles good candidates for this application, considering the high natural abundance and the low toxicity of silicon.

In conclusion, we have measured absorption spectra of individual silicon nanocrystals in the visible range and found an energy structure consisting of several broad peaks, successfully reproduced by atomistic calculations. The origin of some peaks was identified as a convolution of transitions from different electron and hole states, including corresponding sublevels. The physics revealed by this single nanodot study of silicon is that the absorption states next to the emission level are still of an indirect band-gap nature, while at higher energies some intermixing with direct band-gap states occurs. For the application part, this large Stokes shift makes silicon nanocrystals attractive as phosphors and biolabels, where material abundance and nontoxicity are clear advantages.

[1] L. W. Wang, L. Bellaiche, S. H. Wei, and A. Zunger, Phys. Rev. Lett. **80**, 4725 (1998).

[2] M. S. Hybertsen, Phys. Rev. Lett. **72**, 1514 (1994).

[3] M. Ediger, G. Bester, A. Badolato, P. M. Petroff, K. Karrai, A. Zunger, and R. J. Warburton, Nat. Phys. **3**, 774 (2007).

[4] I. Sychugov, J. Valenta, K. Mitsuishi, M. Fujii, and J. Linnros, Phys. Rev. B **84**, 125326 (2011).

[5] M. Bayer, O. Stern, P. Hawrylak, S. Fafard, and A. Forchel, Nature (London) **405**, 923 (2000).

[6] A. Franceschetti and A. Zunger, Europhys. Lett. **50**, 243 (2000).

[7] E. Dekel, D. Gershoni, E. Ehrenfreund, D. Spektor, J. M. Garcia, and P. M. Petroff, Phys. Rev. Lett. **80**, 4991 (1998).

[8] B. Urbaszek, R. J. Warburton, K. Karrai, B. D. Gerardot, P. M. Petroff, and J. M. Garcia, Phys. Rev. Lett. **90**, 247403 (2003).

[9] S. A. Empedocles, D. J. Norris, and M. G. Bawendi, Phys. Rev. Lett. **77**, 3873 (1996).

[10] M. Ben-Chorin, B. Averboukh, D. Kovalev, G. Polisski, and F. Koch, Phys. Rev. Lett. **77**, 763 (1996).

[11] T. Kitasako and K.-i. Saitow, Appl. Phys. Lett. **103**, 151912 (2013).

[12] D. Hessman, P. Castrillo, M. E. Pistol, C. Pryor, and L. Samuelson, Appl. Phys. Lett. **69**, 749 (1996).

[13] Y. Toda, O. Moriwaki, M. Nishioka, and Y. Arakawa, Phys. Rev. Lett. **82**, 4114 (1999).

[14] H. Htoon, P. J. Cox, and V. I. Klimov, Phys. Rev. Lett. **93**, 187402 (2004).

[15] F. Sangghaleh, B. Bruhn, T. Schmidt, and J. Linnros, Nanotechnology **24**, 225204 (2013).

[16] C.-C. Tu, J. H. Hoo, K. F. Boehringer, L. Y. Lin, and G. Cao, Opt. Express **22**, A276 (2014).

[17] H. Nishimura *et al.*, J. Cell Biol. **202**, 967 (2013).

[18] S. Saeed, E. M. L. D. de Jong, K. Dohnalova, and T. Gregorkiewicz, Nat. Commun. **5**, 4665 (2014).

[19] F. Sgrignuoli, P. Ingenhoven, G. Pucker, V. D. Mihailetchi, E. Froner, Y. Jestin, E. Moser, G. Sanchez, and L. Pavesi, Sol. Energy Mater. Sol. Cells **132**, 267 (2015).

[20] M. T. Trinh, R. Limpens, W. D. A. M. de Boer, J. M. Schins, L. D. A. Siebbeles, and T. Gregorkiewicz, Nat. Photonics **6**, 316 (2012).

[21] See Supplemental Material at http://link.aps.org/supplemental/10.1103/PhysRevB.93.161413 for experimental and calculation details.

[22] I. Sychugov, A. Fucikova, F. Pevere, Z. Yang, J. G. C. Veinot, and J. Linnros, ACS Photonics **1**, 998 (2014).

[23] F. Pevere, I. Sychugov, F. Sangghaleh, A. Fucikova, and J. Linnros, J. Phys. Chem. C **119**, 7499 (2015).

[24] F. Sangghaleh, I. Sychugov, Z. Yang, J. G. C. Veinot, and J. Linnros, ACS Nano **9**, 7097 (2015).

[25] J.-W. Luo, P. Stradins, and A. Zunger, Energy Environ. Sci. **4**, 2546 (2011).

[26] L. W. Wang and A. Zunger, Phys. Rev. B **54**, 11417 (1996).

[27] H. X. Fu, L. W. Wang, and A. Zunger, Phys. Rev. B **57**, 9971 (1998).

[28] J. W. Luo, S. S. Li, J. B. Xia, and L. W. Wang, Appl. Phys. Lett. **88**, 143108 (2006).

[29] L. W. Wang and A. Zunger, Phys. Rev. B **51**, 17398 (1995).

[30] V. Mlinar and A. Zunger, Phys. Rev. B **80**, 205311 (2009).

[31] I. Sychugov, Y. Nakayama, and K. Mitsuishi, Nanotechnology **21**, 5, 285307 (2010).

[32] J. Valenta, M. Greben, Z. Remes, S. Gutsch, D. Hiller, and M. Zacharias, Appl. Phys. Lett. **108**, 023102 (2016).

[33] W. A. Thornton, J. Opt. Soc. Am. **61**, 1155 (1971).

[34] X. Wang, X. Yan, W. Li, and K. Sun, Adv. Mater. **24**, 2742 (2012).

[35] E. Petryayeva, W. R. Algar, and I. L. Medintz, Appl. Spectrosc. **67**, 215 (2013).

[36] B. Lee, J. W. Luo, N. Neale, M. Beard, D. Hiller, M. Zacharias, P. Stradins, and A. Zunger, Nano Lett. **16**, 1583 (2016).

Supplemental Material

Single-dot Absorption Spectroscopy and Theory of Silicon Nanocrystals

Ilya Sychugov, Federico Pevere, Jun-Wei Luo, Alex Zunger, Jan Linnros

A. Experiment: Silicon nanocrystals in an oxide matrix were produced by plasma etching and oxidation of low-doped silicon-on-insulator (SOI) wafers at 900°C for 30 seconds. It was found from transmission electron microscope (TEM) images that the samples contain nanocrystals of a shape close to spherical, as well as faceted nanoparticles [30]. The samples were placed on a conventional inverted wide-field microscope (Zeiss) and excited using epifluorescence (bright-field) geometry. The emitted light was collected by a X100 (0.9 NA, for room temperature) or by a X63 (0.75 NA, for low temperature) objective lens and detected by a thermoelectrically cooled EM-CCD camera (Andor, iXon3). For low-temperature measurements (70 K) the samples were mounted on the cold finger of a liquid-nitrogen flow cryostat (Oxford Instruments). Photoluminescence excitation measurements were performed using a laser-driven Xe lamp white light source (Energetic) with an attached wavelength-selecting monochromator (Princeton Instruments). Appropriate long-pass filters were used to cut off second-order harmonics. Unlike ordinary Xe lamps, which suffer from temporal and spatial instabilities of the discharge, the small size of the electrodeless plasma ($\sim$ 100 µm), set here by the external laser, provided superior stability ($<$ 0.1% output power fluctuations measured over hours). The full width at half maximum (FWHM) of the excitation spectral line was $\sim$ 6 nm, defined by the monochromator out-coupling fiber diameter (0.5 mm). This corresponds to 20 – 60 meV bandwidth of the excitation beam in the probed spectral range (2.0 – 3.5 eV), which allowed collecting at least 35-40 data points for the absorption spectrum. The source provided an excitation power of $\sim$ 0.1 mW per single excitation line (as measured by an optical power meter at the sample position). The beam was focused to a spot of $\sim$ 30 µm diameter, where a particular quantum dot of interest was moved to using a remote micro positioning system. The emission range of nanocrystal PL that could be probed in this experiment was from 1.7 to 1.9 eV, limited by the system detection sensitivity and by the epifluorescence filter cube, respectively. The PL signal was then extracted from the recorded images for every excitation wavelength by integrating the signal area ($\sim$ 6×6 pixels) and subtracting the background taken from the region next to the quantum dot. Typically, to

increase the signal-to-noise ratio, results of two separate spectral scans were averaged. To acquire photoluminescence spectrum of a nanocrystal, the emitted light was dispersed in a spectrometer (Andor Shamrock) and recorded with the same CCD camera.

To extract the energy dependence of the absorption cross-section σ (cm^2) from the measured PL intensities, first we note that for a quantum dot below saturation the measured signal rate I_{det} (counts/sec) is directly proportional to the excitation photon flux Φ_{exc} (photons/cm^2/sec):

$$I_{det} = \sigma \cdot QY \cdot D \cdot \Phi_{exc} \tag{1},$$

where QY is the nanocrystal quantum yield and D is the system detectivity (counts/photon). We have experimentally verified the linearity of the signal rate dependence on the excitation power for the studied nanocrystals both at room and at low temperatures. Second, according to the Kasha-Vavilov rule, the quantum yield is excitation energy independent in this energy range, as it was recently verified experimentally for ligand-passivated Si nanocrystals [21]. Finally, the system detectivity is also a constant in this respect, since we detect the same emission line for all the excitation energies E. Thus the only varying parameters, which contribute to the energy dependence of the absorption cross-section σ (E), are the detected PL intensity I_{det} (E) and the excitation photon flux Φ_{exc} (E):

$$\sigma(E) \sim \frac{I_{det}(E)}{\Phi_{exc}(E)} \tag{2}.$$

To obtain luminescence decay and rise times, necessary to find absolute values of the absorption cross-section, a modulated 405 nm laser diode (Omicron) was used for the excitation. In this experiment the photoluminescence signal was collected by an avalanche photodiode (ID Quantique) connected to another output port of the same microscope [S1]. In general, it can be shown from population rate equations that the luminescence rise rate Γ_{rise} is directly proportional to the excitation photon flux Φ_{exc} [S2]:

$$\Gamma_{rise} = \sigma \cdot \Phi_{exc} + \Gamma_{decay} \tag{3},$$

where Γ_{decay} is the luminescence decay rate (typical exciton lifetime is a few microseconds [15]). Thus the slope of this linear dependence yields the absorption cross-section [S1].

We used deconvolution fitting to extract information on the absorption peaks from experimental curves. In the table below the extracted fitting parameters are presented for Si nanodots measured at low temperature.

	Dot N1	Dot N2	Dot N3	Dot N4	Dot N5
Emission, eV	1.705	1.750	1.785	1.820	1.890
Peak N1, eV	2.28±0.11	2.30±0.10	2.32±0.15	2.25±0.08	2.32±0.08
Peak N2, eV	2.68±0.19	2.70±0.18	2.64±0.14	2.67±0.18	2.69±0.17
Peak N3, eV	2.96±0.13	2.97±0.12	2.92±0.11	2.94±0.12	2.94±0.10
Peak N4, eV	3.37±0.19	3.32±0.18	3.36±0.33	3.28±0.22	3.32±0.23

Table S1. *Absorption peak positions and their half-width at half maxima for Si nanodots measured at 70 K.*

To evaluate possible stress in the studied nanocrystals we performed Fourier transform analysis of the high resolution TEM images. An example is shown in Figure S1.
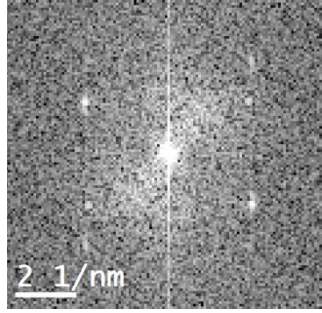

Figure S1. *Fourier transform of the nanocrystal TEM image from Figure 2, left. Four symmetric peaks corresponding to {111} Si planes are visible.*

The interplanar distance for (111) planes in Si (lattice constant a = 5.43 Å) is d = $\frac{a}{\sqrt{h^2 + k^2 + l^2}} = \frac{5.43}{\sqrt{3}}$ = 3.135 Å, or 3.19 nm^{-1} in the reciprocal space. The measured interplanar distance from Figure S1 is 3.20±0.03 nm^{-1}, indicating low strain in the nanocrystal.

B. Atomistic Theory: We obtain the single-particle eigenstates $\{\varepsilon_i;\ \psi_i(r)\}$ of the Si NCs from direct diagonalization, in a basis set of plane-wave functions, of the Schrödinger equation [24]:

$$\left(-\frac{\hbar^2}{2m}\nabla^2 + V(\mathbf{r})\right)\psi_i(\mathbf{r}) = \epsilon_i\psi_i(\mathbf{r})$$

(4),

where the crystal potential of the NC plus its matrix are both described as a superposition of atomic screened (semi-empirical pseudopotential) potentials υ_α of atom type at each atomic site $R_{\alpha,n}$ within the lattice site n: $V(\mathbf{r}) = \sum_{\alpha,n} \upsilon_\alpha(\mathbf{r} - \mathbf{R}_{\alpha,n})$. The pseudopotentials υ_α are fitted to experimental transition energies, effective masses, and deformation potentials of the bulk material [28]. This atomistic empirical pseudopotential method takes into account inter-band coupling, inter-valley coupling (coupling between different parts of the Brillouin zone), and spin-orbit coupling. Although bulk Si has a very small spin-orbit interaction reflecting as small spin-orbit energy of 44 meV and its effect on the calculated spectra is expected to be negligible, in our atomistic calculations we still include the treatment of spin-orbit interaction. Because the continuum k·p effective mass approaches are extensively used in nanoscience and, in fact, the atomistic features of nanostructures usually play important roles in inter-band and inter-valley coupling, here we use "atomistic theory" term to emphasize the difference between our method with continuum k·p effective mass approach.

The no-phonon optical absorption spectrum $\alpha(\hbar\omega)$ in single-particle basis is calculated, given the dipole transition matrix $\overline{P}_{vc} = <v|\hat{e} \cdot \mathbf{p}|c>$, according to the Fermi-golden rule:

$$\alpha(\hbar\omega) = \left(\frac{2\pi e}{m_0\omega}\right)^2 \sum_v \sum_c |\overline{P}_{vc}|^2 exp\left[-\left(\frac{\hbar\omega - E_{vc}}{\lambda}\right)^2\right] \tag{5.}$$

Here $E_{vc} = \epsilon_c - \epsilon_v$ is the transition energy from hole state υ to electron state c, m_0 is the free-electron mass, and e is the free-electron charge, and λ represents the spectral line broadening. The many-body effect including Coulomb and exchange interactions and electron-electron correlation is solved using a configuration interaction (CI) approach [3]. The many-body exciton wavefunction Ψ^γ is constructed as a linear combination of a set of Slater determinants that are composed of N_v hole and N_c electron single-particle wave functions $\psi_i(\mathbf{r})$:

$$\Psi^\gamma = \sum_{v=1}^{N_v} \sum_{c=1}^{N_c} A_{v,c}^\gamma \Phi_{v,c} \tag{6.}$$

The coefficients $A_{v,c}^\gamma$ of the CI expansion are calculated by diagonalizing the CI Hamiltonian for a single exciton:
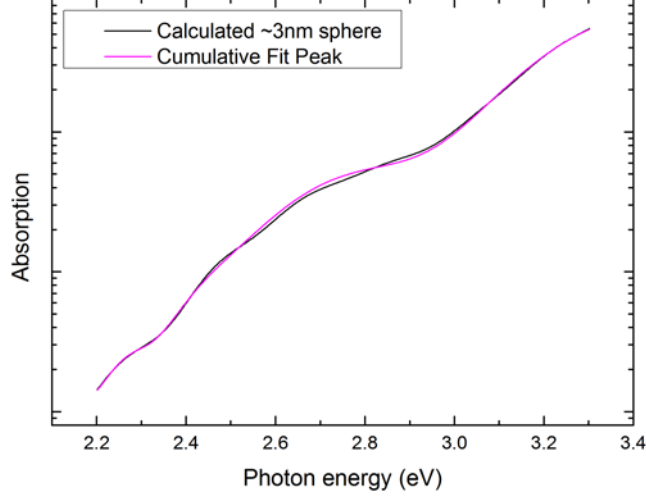
Figure S2. *Calculated absorption curve for a ~ 3 nm diameter Si nanocrystal (black) and its deconvolution with 4 peak Gaussian fitting (magenta). Coefficient of determination (adjusted R-squared) of the fitting is 0.9997.*

$$H_{vc,v'c'} = <\Phi_{v,c}|H_{CI}|\Phi_{v',c'}> = (\varepsilon_c - \varepsilon_v)\delta_{v,v'}\,\delta_{c,c'} - J_{vc,v'c'} + K_{vc,v'c'} \qquad (7),$$

where the Coulomb and exchange integrals $J_{vc,v'c'}$ and $K_{vc,v'c'}$ are given by

$$J_{vc,v'c'} = e^2 \sum_{\sigma,\sigma'} \int\int \frac{\psi_v(\mathbf{r},\sigma)\psi_c(\mathbf{r}',\sigma')\psi_{v'}(\mathbf{r},\sigma)\psi_{c'}(\mathbf{r},\sigma')}{\overline{\epsilon}(\mathbf{r},\mathbf{r}')|\mathbf{r}-\mathbf{r}'|}d\mathbf{r}d\mathbf{r}' \qquad (8a)$$

$$K_{vc,v'c'} = e^2 \sum_{\sigma,\sigma'} \int\int \frac{\psi_v(\mathbf{r},\sigma)\psi_c(\mathbf{r}',\sigma')\psi_{c'}(\mathbf{r},\sigma)\psi_{v'}(\mathbf{r},\sigma')}{\overline{\epsilon}(\mathbf{r},\mathbf{r}')|\mathbf{r}-\mathbf{r}'|}d\mathbf{r}d\mathbf{r}' \qquad (8b).$$

The Coulomb potential in Eqs. (8a) and (8b) is screened using a position-dependent and size-dependent screening function $\overline{\varepsilon}(r,r')$ [S3]. In theoretical simulation, we use a two-step procedure to solve the excitonic properties of QDs. The first step is to obtain the single-particle pure electron and pure hole eigenstates by solving the atomic pseudopotential Schrodinger equation. The second step considers electron-hole excitonic effects by using configuration interaction method to solve the many-body interaction. Since Coulomb interactions bound an electron and a hole to form an exciton, excitonic states are admixture of electron and hole. Giving the dipole matrix and energy levels of exciton states, we are ready to obtain the absorption spectrum in many-body level [24].

For the modelling of matrix a fictitious, lattice-matched barrier material having a wide band gap and large type-I band offsets with respect to bulk Si was introduced. Hence, the Si QDs calculated in this paper are a strain- and defect-free system relevant to the probed here optically active strain-free nanocrystals (Figure S1). The matrix material reproducing the experimentally measured bandgap of Si QDs in SiO_2 for a wide range of QD size was used. For more details see Ref. [24]. Since the modeling of the matrix is a fictitious, lattice-matched barrier, there is no need to relax the atomic positions. To avoid electronic interaction between QD with its periodic image the supercell containing both a Si QD and the matrix was set to be large (surface-to-surface distance between QD with its image is about 5 lattice constants). Eigen energies were found to converge at such separations. A 1 nm edge-to-edge distance is large enough to avoid the effects of supercell size even for as small as 2 nm diameter Si NC [24].

For the purpose of analysis only, we expand NC wavefunctions by a set of Bloch states of underlying perfect Si crystal:

$$\psi_i(\mathbf{r}) = \sum_{n,\mathbf{k}} c_i(n,\mathbf{k}) \phi_{n,\mathbf{k}}(\mathbf{r}) \tag{9},$$

and we obtain the "majority representation" decomposition of the NC states by summing over the coefficients $c_i(n, \mathbf{k})$ to obtain the projection of the NC wave function i on each k point in the bulk Si Brillouin zone: $p_i(\mathbf{k}) = \sum_n |c_i(n,\mathbf{k})|^2$. An auxiliary quantity useful for analysis is the weight functions ω_i^Γ, ω_i^X, and ω_i^L, which are defined by summing $p_i(\mathbf{k})$ over the k points contained in a spherical region around Γ, L, and X, respectively:

$$w_i^{\Gamma(X,L)} = \sum_{\mathbf{k} \in \Omega_{\Gamma(X,L)}} p_i(\mathbf{k}) \tag{10}.$$

The spheres Ω_Γ, Ω_X, and Ω_L in the fcc Brillouin zone have the same radius of $0.5(2\pi/a)$. These quantities represent projections of the quantum dot states to Γ, X, and L bulk components.

Supplemental References

[S1] F. Sangghaleh, B. Bruhn, I. Sychugov, J. Linnros, "Optical Absorption Cross Section and Quantum Efficiency of a Single Silicon Quantum Dot." *Proc. of SPIE* **8766**, 876607 (2013).

[S2] F. Priolo, G. Franzo, D. Pacifici, V. Vinciguerra, F. Iacona and A. Irrera "Role of the Energy Transfer in the Optical Properties of Undoped and Er-doped Interacting Si Nanocrystals" *J. Appl. Phys.* **89**, 264-272 (2001).

[S3] A. Franceschetti, H. Fu, L. W. Wang, and A. Zunger "Many-body Pseudopotential Theory of Excitons in InP and CdSe quantum dots" *Phys. Rev. B* **60**, 1819 (1999).